AGU PUBLICATIONS

JGR

Journal of Geophysical Research: Solid Earth

RESEARCH ARTICLE
10.1002/2017JB014931

Key Points:
- Laboratory study on the frictional properties of Opalinus Clay, a host rock for nuclear waste storage, was presented
- Faults within the Opalinus Clay formation are mechanically weak
- Velocity strengthening and lack of restrengthening during interseismic periods predict aseismic fault slip behavior

Correspondence to:
L. F. Orellana,
felipe.orellana@epfl.ch

Citation:
Orellana, L. F., Scuderi, M. M., Collettini, C., & Violay, M. (2018). Frictional properties of Opalinus Clay: Implications for nuclear waste storage. *Journal of Geophysical Research: Solid Earth*, *123*, 157–175. https://doi.org/10.1002/2017JB014931

Received 31 AUG 2017
Accepted 12 DEC 2017
Accepted article online 21 DEC 2017
Published online 12 JAN 2018

Frictional Properties of Opalinus Clay: Implications for Nuclear Waste Storage

L. F. Orellana[1], M. M. Scuderi[2,3], C. Collettini[2,3], and M. Violay[1]

[1]Laboratory of Experimental Rock Mechanics, EPFL, ENAC, Lausanne, Switzerland, [2]Dipartimento di Scienze della Terra, Università degli Studi La Sapienza, Rome, Italy, [3]Istituto Nazionale di Geofisica e Vulcanologia, Rome, Italy

Abstract The kaolinite-bearing Opalinus Clay (OPA) is the host rock proposed in Switzerland for disposal of radioactive waste. However, the presence of tectonic faults intersecting the OPA formation put the long-term safety performance of the underground repository into question due to the possibility of earthquakes triggered by fault instability. In this paper, we study the frictional properties of the OPA shale. To do that, we have carried out biaxial direct shear experiments under conditions typical of nuclear waste storage. We have performed velocity steps (1–300 μm/s) and slide-hold-slide tests (1–3,000 s) on simulated fault gouge at different normal stresses (4–30 MPa). To establish the deformation mechanisms, we have analyzed the microstructures of the sheared samples through scanning electron microscopy. Our results show that peak (μ_{peak}) and steady state friction (μ_{ss}) range from 0.21 to 0.52 and 0.14 to 0.39, respectively, thus suggesting that OPA fault gouges are weak. The velocity dependence of friction indicates a velocity strengthening regime, with the friction rate parameter ($a - b$) that decreases with normal stress. Finally, the zero healing values imply a lack of restrengthening during interseismic periods. Taken together, if OPA fault reactivates, our experimental evidence favors an aseismic slip behavior, making the nucleation of earthquakes difficult, and long-term weakness, resulting in stable fault creeping over geological times. Based on the results, our study confirms the seismic safety of the OPA formation for a nuclear waste repository.

1. Introduction

Based on its favorable hydro-mechanical properties, the kaolinite-bearing Opalinus Clay formation (OPA) has been selected as suitable candidate for the long-term underground storage of radioactive waste. Located in the northern part of Switzerland, this shale formation is characterized by a very low permeability (10^{-19} to 10^{-21} m^2), a self-sealing capacity (i.e., the spontaneous reduction of fracture permeability by hydro-mechanical, hydro-chemical, and/or hydro-bio-chemical processes (Bock et al., 2010)), and advantageous geo-chemical properties that allow the formation to prevent the migration of radionuclides (Bossart et al., 2017).

To ensure the safety of any deep geological repository, the host rocks need to be seismically safe over geological time scales (~300.000 years, the time needed for radioactivity decay). However, within the OPA formation, various tectonic fault systems have been identified. Among them, the "Main Fault" is a major thrust fault that intersects the Mont Terri Underground Laboratory (MTUL), an international research consortium devoted to the development of a better understanding for the concept of deep geological disposal of nuclear waste (Figure 1) (Bossart et al., 2017; Nussbaum et al., 2011).

Clearly, the presence of various tectonic fault systems put into question the suitability of the formation for the purpose of nuclear waste repositories. Moreover, during the life of the deep geological repository, changes of the surrounding stress field can modify the hydro-mechanical and geo-mechanical properties of the host formation (Popp et al., 2008; Tsang et al., 2012). Natural perturbations (e.g., earthquakes and hydrologic boundary conditions) or engineering activities (e.g., tunnel excavations) may perturb the local stress field, and hence, influence the response of a fault system by triggering natural or induced earthquakes that can potentially damage the underground storage facilities (Hashash et al., 2001; Perfettini & Ampuero, 2008; Wang et al., 2001). The infrastructure loss may be then followed by radionuclide leakages to the surface, contaminating aquifers, causing environmental harm, and posing a direct risk to the health of the nearby population.

In this paper, we present results of an experimental study on the frictional properties of the Opalinus Clay formation from borehole samples retrieved from the Main Fault. To do this, we performed friction experiments at low-slip velocities (3 to 300 μm/s) in a double shear direct configuration under representative nuclear

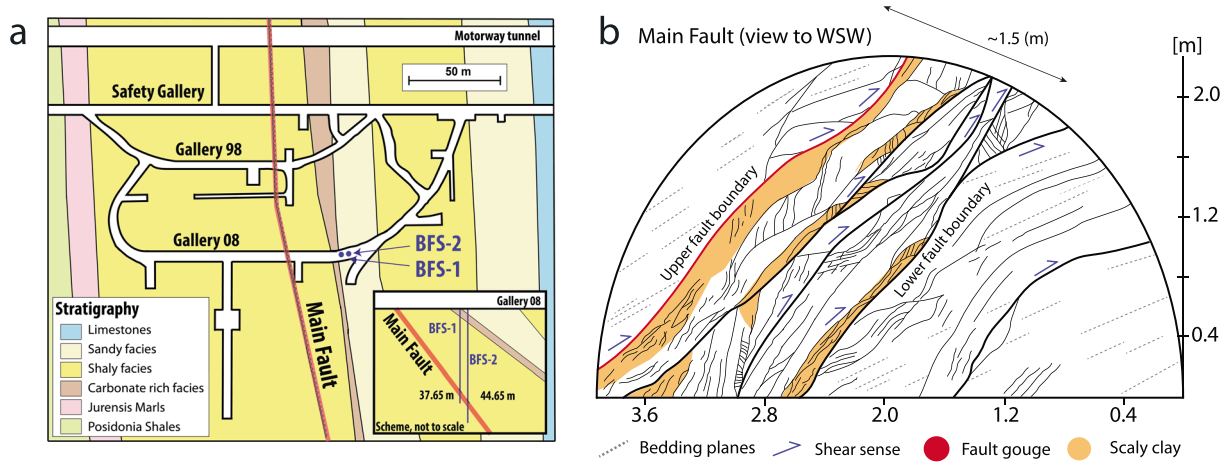

Figure 1. (a) Simplified geological plan view map of the Mont Terri Laboratory (MTUL) modified after Nussbaum et al. (2011). Figure 1a shows the distribution of the different facies within the Opalinus Clay Formation (see legend) and location of boreholes BFS-1 and BFS-2. Inset is a scheme not to scale of the boreholes drilled through the Main fault zone. (b) Scheme of the Main Fault intersected in gallery 98 at MTUL modified after Nussbaum et al. (2011). The "Main Fault" zone is about 0.8–0.9 to 3 m thick. The lower and upper fault boundaries have a dip of 55–60° to the SSE. Bedding planes dips in the same direction with a 15° angular difference (Nussbaum et al., 2011).

waste repository conditions (4 to 30 MPa normal stress). Here, for the first time, we report a full collection of results regarding the frictional properties of the Opalinus Clay formation. By doing so, we discuss the potential for fault reactivation; the associated slip behavior, i.e., stable or unstable; and its implications on its use as a nuclear waste repository.

Previous works on friction have emphasized the role of mineralogy on the frictional behavior of rocks. In addition to the grain size and environmental conditions (temperature, surrounding stresses, presence and chemistry of water, and others), the mineralogy of the fault gouge has proved to be a critical parameter controlling the frictional behavior and slip stability of faults. Moreover, when fault gouges contain certain clay minerals, they exhibit a generally weak frictional strength relative to the Byerlee's rule (Byerlee, 1978; Shimamoto & Logan, 1981). Indeed, laboratory experiments on clay-rich gouges have shown a large variety of friction values ranging from 0.1 to 0.6 (Bird, 1984; Haines et al., 2014; Ikari et al., 2011; Kohli & Zoback, 2013; Niemeijer & Collettini, 2013; Numelin et al., 2007; Saffer et al., 2001, 2012; Smith & Faulkner, 2010; Tembe et al., 2010; Tesei et al., 2012, 2014; Tsutsumi et al., 2011). In the context of the rate and state constitutive laws (Dieterich, 1979; Marone, 1998; Ruina, 1983; Scholz, 1998), it has also been shown that the vast majority of clays show velocity strengthening behavior at slow slip velocities (0.1–100 μm/s), and low frictional healing rates.

Among clays, the number of experiments on the frictional properties of kaolinite-rich gouges is scarce in the literature, especially when compared to the extensive attention devoted to illite, smectite, or montmorillonite minerals. Moreover, while results on the frictional strength of kaolinite-rich gouges are more common, data on the velocity dependence of friction and fault healing are limited. In terms of frictional strength, kaolinite-rich samples have shown diverse values ranging between 0.22 to 0.55 and 0.4 to 0.85 for wet and dry conditions, respectively (Bos et al., 2000; Bos & Spiers, 2000; Brantut et al., 2008; Carpenter et al., 2016, 2015; Crawford et al., 2008; Fang et al., 2017; Moore & Lockner, 2004; Morrow et al., 2000).

Regarding the frictional stability and fault healing, the samples from the Northeast Boundary Fault composed of ~25% of kaolinite + chlorite exhibited an uniform velocity strengthening behavior and healing rates between 0.0035 and 0.007 (Carpenter et al., 2015). Frictional healing tests on kaolinite/halite mixtures have shown that the presence of kaolinite inhibited halite to halite contact, reducing the healing capacity of the gouge material to a very small restrengthening rate (Bos & Spiers, 2000). Recently, in the context of CO_2 sequestration, one shear experiment where two blocks of intact Opalinus Clay slide against each other was carried out at 3 MPa effective normal stress and sliding velocities of 1 and 10 μm/s (Fang et al., 2017). The authors have shown a velocity strengthening regime and a steady state friction value equal to 0.5.

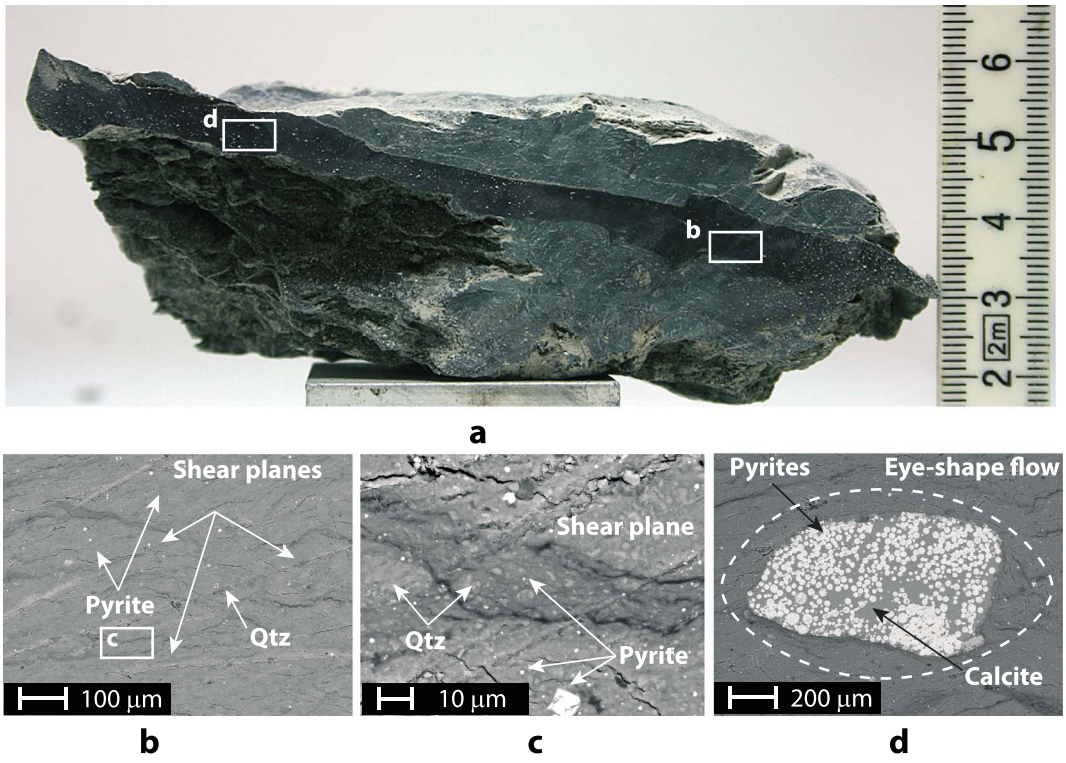

Figure 2. A centimeter-scale sample (recovered from borehole BFS2) and BSE images of Opalinus Clay gouge. (a) Hand sample of Opalinus Clay gouge. Gouge thickness is about 1 cm. (b) The homogenous clay matrix has fine grain size (~7 μm). We observe the ubiquitous presence of quartz (Qtz), smaller proportions of pyrite and calcite minerals, and subhorizontal sets of interconnected shear planes. The white box indicates the positon of Figure 2c. (c) A subhorizontal shear plane underlined by the orientation of clay platelets. (d) Clay matrix flowing around rigid, subrounded calcite crystal forming an eye-shape flow pattern perturbation (Passchier & Trouw, 2005). In this case, several pyrite framboids are on the surface of the calcite mineral.

Unfortunately, a more comprehensive work on the frictional properties of the OPA fault rocks is lacking so far. This is the focus of our study. We integrate mechanical data and observations of microstructural deformation to provide a thorough analysis of the frictional behavior of the OPA fault rocks. By doing so, we provide results on its frictional strength, stability, and healing behavior.

2. The Opalinus Clay-Fault Gouge

At the MTUL, the BSF-1 and BSF-2 boreholes (Figure 1a, inset) were drilled in gallery 08 intersecting the Main Fault. Both intact and faulted samples were recovered. Fault core samples contain an arrangement of different structural elements, including an anastomosing network of scaly clays and fractures, calcite veins, undisturbed blocks, shear zones, and a series of planes containing fault gouges (Laurich et al., 2014; Nussbaum et al., 2011).

Within the fault core, the Opalinus Clay-fault gouges (Figure 2) appear as dark and partially continuous bands of 8–15 mm in thickness, surrounded by deformed rock, including portions of scaly clay. The darker color originates from the reduction of the particle size (~7 μm) and smaller calcite content compared to the protolith (Laurich et al., 2014). Some particular elements can be recognized within the fault gouge, including a texture of very fine and homogeneous grain size, and the ubiquitous presence of quartz minerals and smaller proportions of pyrite and calcite minerals (Figure 2b). The fault gouge is layered through a regular and subhorizontal fabric (Figure 2b) linked to interconnected shear planes underlined by the orientation of clay platelets (Figure 2c). We also observed isolated and relatively large, rigid, subrounded minerals, often quartz, but also calcite minerals inside the clay-rich gouge (Figure 2d). Their presence developed an eye-shape flow pattern perturbation (i.e., shear flow around a round object in simple shear flow (Passchier & Trouw, 2005)) highlighting the apparent movement of clay minerals around those large fragments.

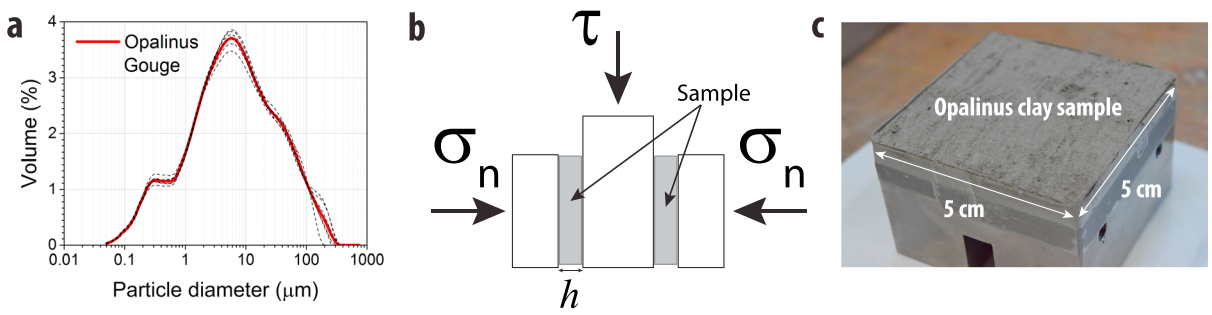

Figure 3. Material and shear configuration. (a) Particle size distribution (PSD) for Opalinus gouge. Ninety percent of the particles are finer than 60 μm, while the average size is 7 μm. (b) Double direct shear configuration used in these experiments. (c) Opalinus Clay samples employed in the experiments on sample holder before shearing.

3. Materials and Methods

3.1. Experimental Samples

To study the frictional properties of the Opalinus Clay gouge, we sheared pulverized samples of intact OPA, hereafter named simulated OPA gouge, at conditions representative of the environment targeted by nuclear waste repositories. We used simulated OPA gouge because natural gouge is difficult to collect and the material recovered from borehole BFS-1 and BFS-2 was not sufficient for our experimental work.

We prepared the simulated gouge sample by crushing and sieving (<300 μm) intact OPA retrieved from the same boreholes. An average grain size of about 7 μm (Figure 3a) was measured using the particle size measurement equipment Malvern Mastersizer S, which is comparable to the gouge grain size of the main fault at MTUL (Laurich et al., 2014).

X-Ray diffraction (XRD) analysis was performed at the Geological Institute of the University of Lausanne, Switzerland. The clay mineral analyses were based on methods outlined by (Kübler, 1987). Sample preparation included, but were not limited to, (a) the disaggregation of the rock, (b) mixing the sample with de-ionize water, (c) removal of the carbonate fraction by the addition of HCl 10% (d) separation of different grain size fractions (<2 μm and 2–16 μm) using the timed settling method based on Stokes law, (e) application of ethylene-glycol onto clays already placed on glass-slide, and finally, (f) the recognition of characteristic XRD peaks of each clay mineral presented in the size fraction.

The mineralogy of the simulated gouge (Table 1) consists of phyllosilicates (~50%), quartz (~23%), calcite (~15%), and smaller proportions of less than 3% of plagioclase—Na, feldspath—K, dolomite, goethite, and pyrite. XRD analysis of intact Opalinus Clay have been reported by other authors where the content of illite-smectite is higher than reported in Table 1 (Fang et al., 2017; Klinkenberg et al., 2009).

Table 1
Bulk Mineral Composition (% Weight) of Opalinus Clay

Mineralogy of the simulated Gouge Opalinus Clay	
Illite-Smectite IS 1	2.25 ± 1.41
Illite-Smectite (2)	0.75 ± 0.29
Mica	10.48 ± 3.55
Chlorite	8.38 ± 2.85
Kaolinite	28.04 ± 0.99
Quartz	23.26 ± 0.70
Feldspar-K	2.40 ± 0.31
Plagioclase-Na	2.34 ± 0.20
Calcite	14.68 ± 0.80
Dolomite	1.19 ± 0.34
Pyrite	1.43 ± 0.30
Goethite	1.90 ± 0.16
Others	2.91 ± 0.39

Note. Four measurements were carried out for the simulated gouge (intact rock from the OPA formation). Results are presented as X ± S, where X is the mean and S the standard deviation. The group Phyllosilicates corresponds to the sum of illite-smectite IS 1, illite-smectite (2), mica, chlorite, and kaolinite.

3.2. Experimental Procedure

We carried out experiments on simulated gouge material to characterize the frictional behavior of the Opalinus Clay as a function of applied normal stress and slip velocity. In our tests, normal stress ranged between 4 and 30 MPa, which are the conditions of interest for nuclear waste repositories (~100–1,000 m depth). We performed experiments using BRAVA installed at INGV, Rome, Italy (Collettini et al., 2014), a biaxial rock deformation apparatus, in the double-direct shear configuration (Figure 3b). In this configuration, two layers of powdered gouge samples (Figure 3c) are sandwiched in a three-steel block assembly, characterized by two side stationary blocks and a central block with a nominal frictional contact area of 5 × 5 cm.

For all the experiments, the gouge layers were constructed using precise leveling jigs to obtain a starting uniform layer thickness of 5 mm.

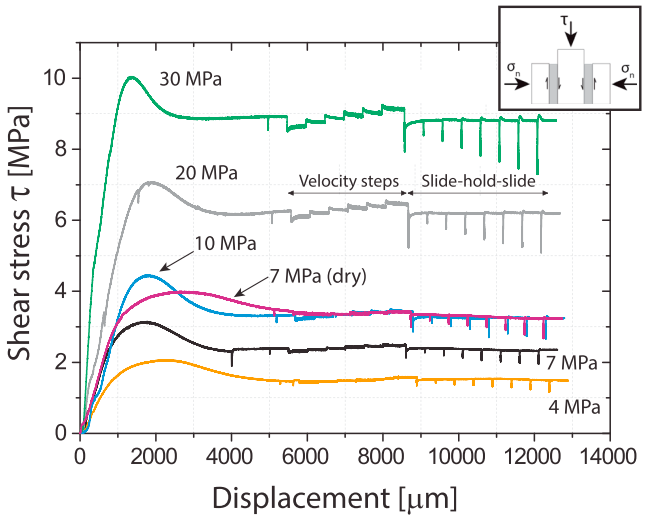

Figure 4. Friction experiments performed on simulated gouge samples of Opalinus Clay at different normal stress (from 4 MPa to 30 MPa). The curves show the evolution of the shear stress (τ) with slip. Experiments show a peak strength followed by a residual value. The curves indicate a low to moderate slip weakening. The weakening is higher at lower normal stress (4, 7, and 10 MPa). Velocity step and slide-hold-slide tests start after shear stress reach a steady value. Inset: Double direct shear configuration used in these experiments.

We used two fast-acting servo-hydraulic rams to apply the horizontal and vertical loads. The applied load was measured via strain gauge load cells (accuracy ±0.03 kN) positioned at the extremity of the hydraulic rams in contact with the sample assembly. We measured the horizontal and vertical displacements by using Linear Variable Displacement Transformers (LVDTs), with an accuracy of ±0.1 μm, referenced to the load frame and the upper side of the ram. The displacement values were corrected by taking into account the machine stiffness for both vertical (928.5 kN/mm) and horizontal (1,283 kN/mm) load frames.

Experiments were run at room temperature (~25°C), on samples that were saturated overnight with fluids at chemical equilibrium with the rock, and at constant 100% relative humidity conditions (RH). To this end, we placed a humidifier inside the BRAVA apparatus to ensure a saturated environment for the samples during deformation. Thus, we prevented them from dehydration. Water humidity was measured with a hygrometer during the experiments. Also, we ran one experiment on dry gouge material (RH = 5%) to evaluate the effect of water saturation.

At the beginning of each test, we applied the normal load and maintained it constant at the target normal stress value via a load feedback control mode. Before shear began, we monitored the thickness of the gouge layer (h) using the horizontal LVDTs (Figure 3b). We measured compaction of the gouge until a constant value of layer thickness was achieved. Then, we started shearing. The initial thickness of the samples (h_o) under load before shearing ranged from 2.7 to 2.3 mm. We determined variation in porosity ($\Delta\varnothing$) during shear via measurement of the change in layer thickness (Δh) assuming that $\Delta\varnothing \approx \frac{\Delta h}{h}$ (Niemeijer et al., 2010; Samuelson et al., 2009).

Each experiment followed a typical computer-controlled displacement history. Shear began with an initial stage at a constant displacement rate of 10 μm/s for ~5.5 mm. During this phase, the sample deformed quasi-elastically until a peak friction value was reached followed by an evolution to a steady state sliding friction (Figure 4).

We calculated the shear stress (τ) dividing the vertical load by the sample surfaces (two gouge layers). Then, we determined the Amonton's friction μ (or frictional resistance) as the ratio of the shear resistance, τ, over the applied normal stress, σ_n.

$$\mu = \frac{\tau}{\sigma_n} \tag{1}$$

However, for a wide range of cohesive surfaces, shear strength might not completely vanish when normal stress is equal to zero, and therefore, a more accurate definition of the coefficient of friction (Lockner & Beeler, 2002) is given by

$$\mu_f = \frac{\tau - S_o}{\sigma_n} \tag{2}$$

where S_o corresponds to an "inherent" shear strength. To provide a more wide-ranging and systemic analysis of our results, in this study, we calculated both the Amonton's friction (μ) and the coefficient of friction for cohesive surface μ_f. Here in this study, when we mention friction, we refer to the Amonton's friction (equation (1)).

To get insight on fault stability, we studied the velocity dependence of friction by imposing different velocity steps (1–300 μm/s) as shown in Figure 5a. For each step, we suddenly increased slip velocity inducing an immediate increase in friction followed by an exponential decay over some critical slip distance (D_c), to a new steady state value of the frictional resistance (Scholz, 2002).

To retrieve the rate and state frictional constitutive parameters, we modeled each velocity step using the Ruina's slip-dependent evolution law (Ruina, 1983). The empirical Ruina's law is defined by the friction relation (equation (3)) and the state evolution law (equation (4)):

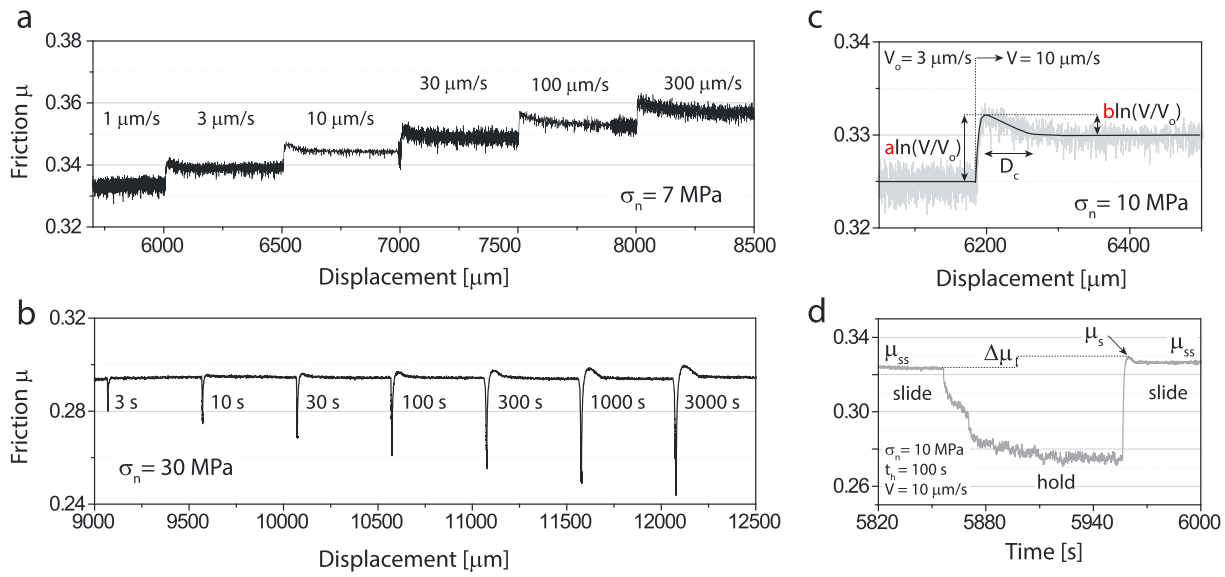

Figure 5. Friction parameter analysis. (a) The coefficient of friction versus displacement during the velocity step sequence. (b) The coefficient of friction versus displacement during the slide hold slide sequence. (c) An example of frictional parameter ($a - b$) measurement. The parameter (a), also known as the direct effect, is proportional to the instantaneous change in friction. The friction parameter (b), also known as the evolution effect, is proportional to the subsequent drop to a new steady state. The black line shows the modeled output of Ruina's slip dependent evolution law. (d) An example of frictional healing ($\Delta\mu$) measurement for experiment i443 (normal stress equal to 10 MPa). The sequence corresponds to 100 s holding time. Frictional healing $\Delta\mu$ is defined as the difference between peak static friction μ_s and the prehold steady state friction μ_{ss}.

$$\mu = \mu_o + a \cdot \ln\left(\frac{V}{V_o}\right) + b \cdot \ln\left(\frac{V_o \cdot \theta}{D_c}\right), \tag{3}$$

$$\frac{d\theta}{dt} = -\frac{V \cdot \theta}{D_c} \cdot \ln\left(\frac{V_o \cdot \theta}{D_c}\right) \tag{4}$$

where μ_o is a constant that represents friction at steady state for a reference velocity V_o, μ is the friction at the new steady state velocity V, and a and b are empirical parameters, also named the direct and evolution effect respectively (Marone, 1998).

As first suggested by Rabinowicz (1951) and then by Dieterich (1979), θ can be interpreted as the average lifetime of contacts, i.e., the average elapsed time since the contacts existing at a given time were first formed (Scholz, 2002). The critical slip distance D_c, at a constant velocity V, is defined as the distance over which friction evolves from a local peak to a steady state. Marone (1998) has pointed out the standard interpretation for D_c as the slip necessary to renew the population of contacts, meaning that contacts are destroyed and replaced by an uncorrelated set (Scholz, 2002). The sliding stability is determined by the friction parameter ($a - b$), defined as

$$a - b = \frac{\Delta\mu_{ss}}{\ln\left(\frac{V}{V_o}\right)} \tag{5}$$

where $\Delta\mu_{ss}$ is the change in the steady state friction upon an immediate change in sliding velocity from V_o to V (Marone, 1998). For neutral or positive rate dependence, $(a - b) \geq 0$, sliding will tend to be stable, and the material will be described as velocity strengthening. Conversely, if the frictional strength decreases upon an increase in sliding velocity, $(a - b) < 0$, any perturbation on the fault will potentially promote slip acceleration. Thus, the system will be considered potentially unstable, and the material will be described as velocity weakening (Scholz, 2002).

We modeled our laboratory data using a fifth-order Runge-Kutta method. It corresponds to an iterative least squares method (Reinen & Weeks, 1993; Saffer & Marone, 2003) that allows us to determine the best fit

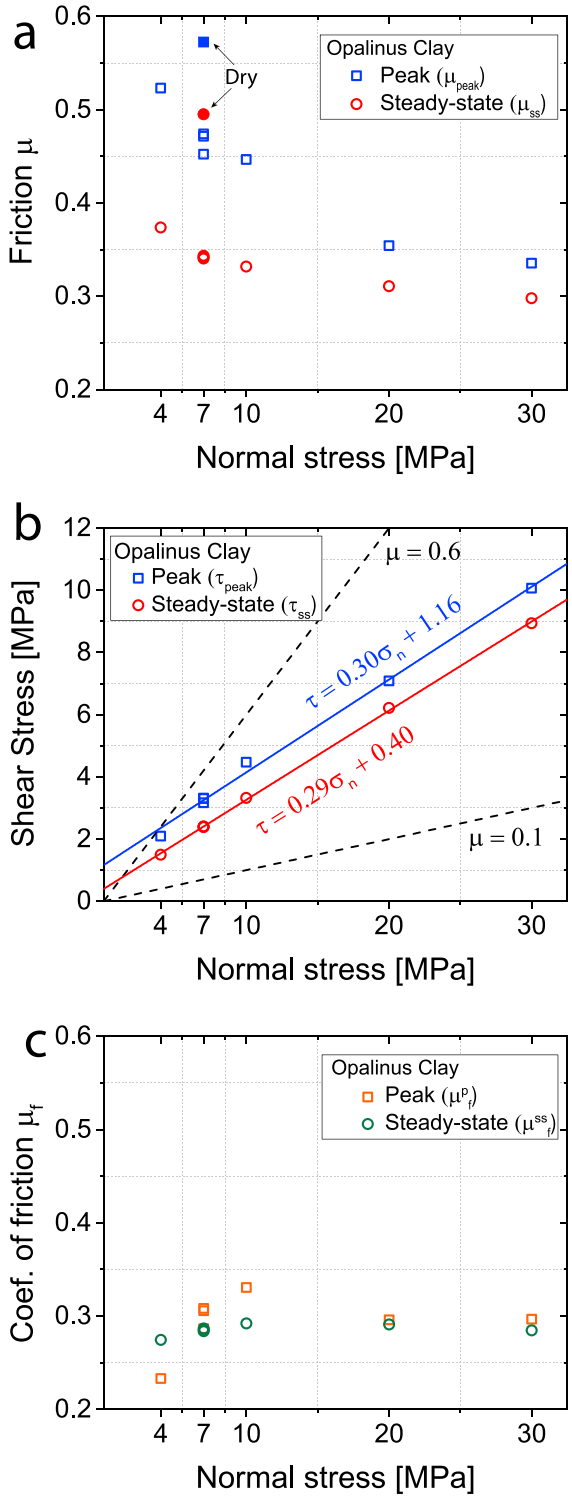

Figure 6. (a) Amonton's friction μ (equation (1)) versus normal stress. In black: peak friction μ_{peak}. In red: steady state friction μ_{ss}. The filled symbols correspond to experiments performed on dry samples. (b) Shear stress versus normal stress. We linearized both peak and steady state shear strength following the linear fit $\tau = \mu_f' \sigma_n + S_o$ as shown in the graph. At the peak, $\mu_{fp}' = 0.30$ and $S_o = 1.16$. At steady state, $\mu_{fss}' = 0.29$ and $S_o = 0.40$. For comparison, we displayed $\tau = 0.6 \cdot \sigma_n$ and $\tau = 0.1 \cdot \sigma_n$ on the chart. (c) The coefficient of friction for coherent surfaces μ_f (equation (2)) at both peak and steady state shear stress.

parameters of the velocity step test, i.e., the critical slip distance D_c, the parameters a and b, and their respective variances derived from the goodness of the model fit to the experimental data.

Slide-hold-slide tests (Figure 5b) were performed to measure the amount of frictional healing ($\Delta\mu$). During these tests, gouge layers were sheared at a constant velocity of 10 μm/s followed by a hold period, t_h, during which the vertical ram is stopped and gouge layers were under quasi-stationary contact. In our tests, the hold period varied between 3 and 3,000 s. After the hold period, the gouge was resheared at 10 μm/s. As is shown in Figure 5c, we observe an increase (or eventually decrease) of friction upon reshear, followed by a decay to the previous steady state value (Scholz, 2002). The amount of frictional healing, $\Delta\mu$, was measured as the difference between the peak friction measured upon reshear after each hold and the prehold steady state friction (Marone, 1998). Frictional healing rates β were calculated as

$$\beta = \frac{\Delta\mu}{\Delta \log_{10}(t_h)} \quad (6)$$

3.3. Microstructural Analysis

At the end of each test, to obtain thin sections parallel to the direction of shear, we recovered parts of the gouge samples, and we embedded them in epoxy resin (London resin). The thin sections of about 30 μm in thickness were prepared at the Dipartimento di Scienze della Terra, Università degli Studi La Sapienza (Rome, Italy). At the Swiss Federal Institute of Technology in Lausanne (EPFL), microstructural observations were conducted on thin sections using secondary electron and backscattered electron (BSE) images; detailed microstructural observations were performed using the scanning electron microscopy FEI XLF30-FEG installed at the Interdisciplinary Centre for Electron Microscopy (EPFL, Switzerland).

4. Results

4.1. Mechanical Data

4.1.1. Frictional Strength

We measured the evolution of shear strength as a function of displacement for gouge samples as presented in Figure 4. We reported the friction μ (Figure 6a) and the inherent shear strength S_o (Figure 6b) and the coefficient of friction μ_f (Figure 6c) values calculated according to equations (1) and (2), respectively.

For all the saturated samples, the shear stress evolved quasi-linearly with displacement until a peak strength was reached (Figure 4). At that point, friction (μ_{peak}) ranged from 0.33 to 0.52 (Figure 6a and Table 2). As shearing continued, shear stress reached a residual value corresponding to a steady state. The steady state condition (achieved between 4 to 5 mm shear displacements) implied steady state friction values (μ_{ss}) that ranged from 0.29 to 0.37 (Figure 6a and Table 2).

We observed a stress weakening in all samples after reaching peak strength (Figure 4). The weakening was about 1 MPa for samples

AGU Journal of Geophysical Research: Solid Earth

10.1002/2017JB014931

Table 2
Frictional Experiments Parameters and Data Summary

Test	Moisture content	Normal Stress (MPa)	Pore pressure (MPa)	Initial porosities Φ (%)	Peak friction μ_{peak}	Steady-state friction μ_{ss}	Up-Step Velocity Steps (μm/s)	Friction parameter *a*	Friction parameter *b*	Friction parameter $(a-b)$	Critical Distance *Dc* (mm)	Sequence of hold times (s)	Healing $\Delta\mu$
i454	Saturated	4	0	27.3	0.523	0.374	3	0.0058	0.0018	0.0041	0.053	3	−0.00013
							10	0.006	0.0018	0.0044	0.046	10	0.00049
							30	0.0066	0.0015	0.0051	0.031	30	−0.00039
							100	0.0056	0.0006	0.005	0.03	1,00	−0.00124
							300	0.0088	0.0016	0.0072	0.003	300	−0.00017
												1,000	−0.00146
												3,000	0.0023
i447	Saturated	7	0	28.7	0.452	0.343	3	0.006	0.0014	0.0047	0.043	3	−0.00021
							10	0.0063	0.0021	0.0042	0.065	10	−0.00011
							30	0.0065	0.002	0.0046	0.079	30	−0.00021
							100	0.0059	0.0031	0.0028	0.113	100	−0.00126
							300	0.007	0.0037	0.0033	0.184	300	−0.00207
												1,000	−0.00096
												3,000	0.00549
i441	Saturated	7	0	25.2	0.472	0.34	3	0.0059	0.0013	0.0047	0.027	3	−0.00058
							10	0.0062	0.0020	0.0042	0.041	10	−0.00103
							30	0.0067	0.0019	0.0048	0.025	30	0.0004
							100	0.0063	0.0022	0.0041	0.034	100	−0.00153
							300	0.0065	0.0018	0.0048	0.109	300	−0.00072
												1,000	0.01058
												3,000	0.02003
i442	Saturated	7	0	27.0	0.474	0.342	3					3	−0.00054
							10					10	0.00014
							30					30	−0.00115
							100					100	−0.00414
							300					300	−0.00644
												1,000	0.00046
												3,000	0.00475
i440	Dry	7	0	27.5	0.572	0.374	3	0.0026	0.0039	−0.0013	0.163	3	0.0021
							10	0.0031	0.0021	0.0009	0.07	10	0.00278
							30	0.0036	0.0011	0.0024	0.068	30	0.00263
							100	0.0032	0.0007	0.0025	0.124	100	0.0039
							300	0.0053	0.0014	0.0039	0.02	300	0.00317
												1,000	0.00443
												3,000	0.00691
i443	Saturated	10	0	22.3	0.447	0.332	3	0.0059	0.0018	0.0041	0.0510	3	0.00003
							10	0.0059	0.0026	0.0033	0.0540	10	0.00055
							30	0.0058	0.0035	0.0023	0.1210	30	0.00152
							100	0.0058	0.0040	0.0019	0.1300	100	0.00616
							300	0.0068	0.0032	0.0036	0.3090	300	0.00228
												1,000	0.00323
												3,000	0.00553
i444	Saturated	20	0	23.0	0.354	0.311	3	0.0059	0.0018	0.0041	0.084	3	0.00002
							10	0.0059	0.0026	0.0033	0.126	10	0.00014
							30	0.0059	0.0035	0.0024	0.159	30	0.00062
							100	0.0058	0.004	0.00187	0.132	100	0.00177
							300	0.0068	0.0032	0.00362	0.174	300	0.00222

Table 2 *(continued)*

Test	Moisture content	Normal Stress (MPa)	Pore pressure (MPa)	Initial porosities Φ (%)	Peak friction μ_{peak}	Steady-state friction μ_{ss}	Up-Step Velocity Steps (μm/s)	Friction parameter *a*	Friction parameter *b*	Friction parameter $(a-b)$	Critical Distance *Dc* (mm)	Sequence of hold times (s)	Healing $\Delta\mu$
												1,000	0.00328
												3,000	0.00314
i445	Saturated	30	0	22.9	0.335	0.298	3	0.0051	0.0016	0.0035	0.133	3	0.00035
							10	0.0053	0.0025	0.0028	0.183	10	0.00058
							30	0.0052	0.004	0.0012	0.396	30	0.00152
							100	0.0053	0.0032	0.0021	0.12	100	0.00262
							300	0.0062	0.0026	0.0037	0.114	300	0.00333
												1,000	0.00464
												3,000	0.00582

sheared at 30, 20, and 10 MPa, while 0.8 and 0.5 MPa for samples sheared at 7 and 4 MPa normal stress, respectively.

The d sample showed peak friction equal to 0.57, steady state friction of 0.37, and a slip weakening of about 0.4 MPa. Figure 6a shows a decrease of both peak and steady state friction when normal stress is increased. Moreover, we observed a larger drop from peak to steady state friction on samples sheared at lower normal stress (4 and 7 MPa) than at higher normal stress.

To calculate the coefficient of friction for cohesive surfaces μ_f (equation (2)), we first fitted the shear stress (Figure 6b) with $\tau = \mu_f^{'}\sigma_n + S_o$, where $\mu_f^{'}$ is the linearized value of the coefficient of friction and S_o the inherent shear strength. While at the peak the inherent shear strength S_o was 1.16, at steady state S_o was equal to 0.40 (Figure 6b). Then, we calculated the coefficient of friction μ_f for each samples following equation (2). Figure 6c shows that the coefficient of friction for cohesive surfaces measured at peak shear stress (μ_f^p) increased with normal stress from 0.23 at 4 MPa to 0.3 at 30 MPa. On the other hand, at steady state shear stress, the steady state coefficients of friction (μ_f^{ss}) were fairly constant over the range of normal stress.

4.1.2. Frictional Stability

Velocity dependence of friction tests on saturated gouge indicated $(a - b)$ values comprised between 0.0072 and 0.0012 (Table 2), i.e., a velocity strengthening regime, with no points in the potentially unstable regime at any sliding velocity. The dry sample sheared at 7 MPa showed a transition from velocity weakening to velocity strengthening at up-step velocity of 10 μm/s.

For saturated gouges, the frictional parameter *a* took values of ~0.006 and showed a nondependent behavior with respect to normal stress. The parameter *b* exhibited an increase from 0.0015 on average at low normal stress (4 MPa) to values of about 0.003 at 10 MPa normal stress (Figure 7b). Thus, the resulting friction rate parameter $(a - b)$ decreased with increasing normal stress (Figure 7a) and no transition to velocity weakening was observed. At all normal stress, the frictional parameters $(a - b)$ did not show a correlation with up-step velocities. For the dry sample sheared at 7 MPa normal stress, the parameter *a* took values of ~0.003. On the other hand, the frictional parameter *b* showed a decrease from 0.004 to 0.001 with increasing up-step velocities from 3 to 300 μm/s.

For saturated gouges, the critical slip distance increased on average from 0.05 to 0.15 mm as normal stress increased (Figure 7c). At 4 MPa normal stress, D_c decreased with increasing displacement and up-step velocity (velocity steps tests were performed at the same up-step velocity sequence in each experiment). At 7 (saturated), 10, and 20 MPa normal stress, D_c slightly increased or remained constant with up-step velocity. At 30 MPa normal stress, there was no general trend. Finally, on dry sample sheared at 7 MPa, D_c decreased with increasing displacement and up-step velocity.

4.1.3. Frictional Healing

Figure 7d shows the healing values ($\Delta\mu$) versus holding times (t_h). Healing values ranged between −0.006 and 0.02 (Table 2). Saturated gouge samples sheared at $\sigma_n > 10$ MPa showed positive healing values and positive healing rates (β). For example, at $\sigma_n = 20$ MPa, $\beta \approx 0.0005$, and at $\sigma_n = 30$ and $\sigma_n = 10$ MPa, the frictional healing rate was equal to $\beta \approx 0.0007$. The dry sample showed positive healing values ranging from 0.002 to 0.006 and a positive healing rate of about $\beta \approx 0.006$.

When normal stress was equal to 4 and 7 MPa, the healing value did not follow the classical log linear fit but showed zero or negative healing values ($\Delta\mu^-$) for hold times <300 s and positive values ($\Delta\mu^+$) for hold times >300 s. To calculate the healing rate, we separated the healing values into two regions considering a critical hold time t_h^* at 300 s. Then, we computed a log linear fit for the healing values contained in each region and we calculated two healing rates for the same experiment. For example, sample sheared at 7 MPa showed a weakening rate $\beta_1^{7\ MPa} \approx -0.0004$ for hold times <300 s and a positive healing rate of about $\beta_2^{7\ MPa} \approx 0.0032$ for hold times >300 s.

4.1.4. Evolution of Porosity and Sample Thinning

Figure 8a shows the evolution of porosity ($\varnothing_t$) during shearing. The initial porosity ($\varnothing_o$) at the start of shearing was ~27% for samples sheared at 4 and 7 MPa, and ~22% for samples sheared at 10, 20, and 30 MPa. At the end of the experiments, porosity showed values of about 18% and 16% for the samples sheared at low (4 and 7 MPa) and high (10, 20, 30 MPa) normal stress, respectively. Accordingly,

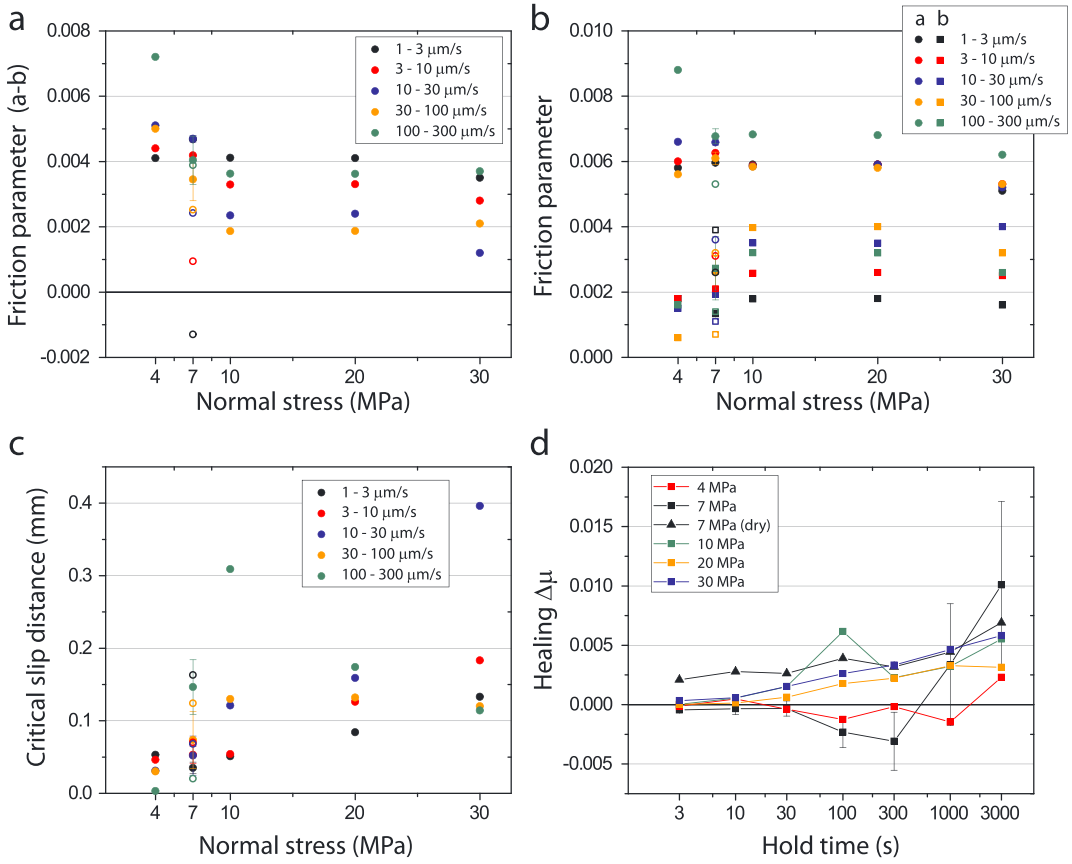

Figure 7. Friction rate parameters for simulated Opalinus Clay gouge. (a) Stability friction parameter ($a - b$) versus normal stress. Gouge samples are characterized by a velocity strengthening behavior meaning ($a - b$) > 0. The parameter ($a - b$) decreased as normal stress increased and ($a - b$) values are nearly close to 0. (b) Evolution of the individual parameters a and b with normal stress. Parameters a and b are represented by a circle and a square, respectively. Parameter b increased when normal stress increased. (c) Critical slip distance D_c versus normal stress. (d) The frictional healing parameter $\Delta\mu$ versus hold time. Experiments were carried out at sliding velocity of 10 μm/s and at different normal stress. The error bars denote the standard deviation of multiple tests and nonfilled symbols referred to results on the dry sample.

sample thinning (h) was greater in samples sheared at 4 MPa ($\Delta h_{4\ \mathrm{MPa}} \sim 1{,}000$ μm) than in samples sheared at 30 MPa ($\Delta h_{30\ \mathrm{MPa}} \sim 600$ μm) due to lower initial compaction of samples sheared at low normal stress.

Following the procedure described in Samuelson et al. (2009), we removed the linear thinning trend from the calculated gouge layer thickness, and then, we determined a corrected value of porosity ($\varnothing_c$). By doing so, we want to emphasize the instantaneous changes in porosity during shearing while analyzing dilation and consolidation during the tests.

During the velocity step tests and based on the evolution of corrected porosity $\varnothing_c$ (red curve), we observed either dilation or consolidation when increasing velocity, i.e., no correlation with the imposed sliding velocity (Figure 8b). During the slide-hold-slide tests and for all samples (Figure 8c), the porosity $\varnothing_t$ (blue curve) showed consolidation during shearing and null dilation or consolidation during hold times. On the other hand, the corrected porosity $\varnothing_c$ (red curve) slightly increased during hold times while it decreased during shearing. The latter was more evident for samples sheared at low normal stress (4 and 7 MPa), as the rate of the porosity changes (drop and recovery) was almost double.

4.2. Microstructural Observations

In this section, we compare the microstructure of postmortem samples sheared at 7 MPa and 30 MPa (Figure 9) following the classification based on the scheme of Logan et al. (1992). The microstructure of the sample sheared at 7 MPa was characterized by the presence of R-shear planes and open cracks parallel

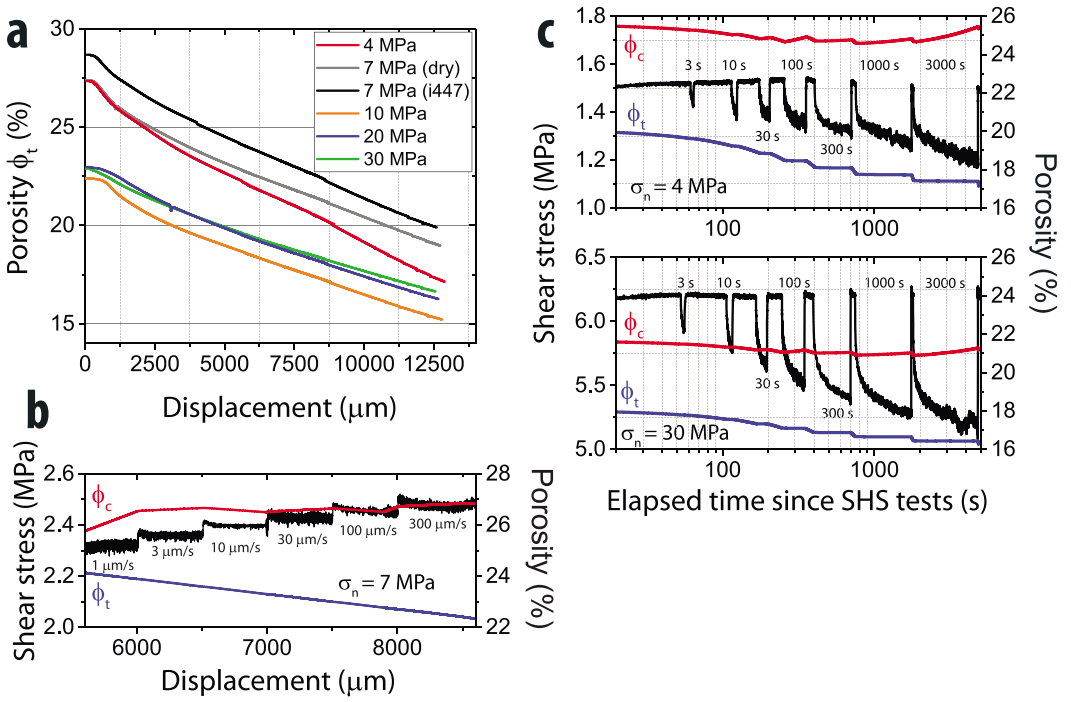

Figure 8. Evolution of porosity. (a) Porosity ($\varnothing_t$) versus shear displacement. On shearing, $\varnothing_t$ monotonically decreases for all samples. The total porosity $\varnothing_t$ decreases from ~27 to ~17% for sample sheared at 4 MPa and from ~22% to ~16% for sample sheared at 30 MPa. (b) Total and corrected porosity versus displacement during velocity step tests for sample sheared at 7 MPa normal stress. (c) Total and corrected porosity versus elapsed time since the beginning of slide-hold-slide tests (in logarithmic scale) for samples sheared at 4 and 30 MPa normal stress. Values of corrected porosity $\varnothing_c$ were treated by removing the linear trend.

to shear direction and orthogonal to the applied normal stress (Figure 9a). Within the Riedel shear bands, clays minerals surrounded calcite and quartz minerals and tended to be distributed subparallel to the R-shear planes (Figure 9c). In the same region, limited fracturing affected calcite grains (Figure 9e).

For experiments performed at 30 MPa normal stress, we observed pervasive R-shear planes, no apparent preferential orientation of cracks, and a significant grain-size reduction within the entire experimental fault (Figure 9b). Riedel shear planes were more numerous and tightly distributed at 30 MPa than at 7 MPa of normal stress (Logan et al., 1992). Here again, clay lamellae surrounded stronger grains, and they were also concentrated along R-shear planes (Figure 9d). The intragranular fracturing of calcite minerals was more pervasive in comparison to experiments at 7 MPa, and fractured grains were always surrounded by clay material (Figure 9f). We did not identify well-developed Y-planes in any of the tested samples.

5. Discussion

5.1. Fault Strength

Whilst the peak friction values (μ_{peak}) of OPA range from 0.33 to 0.52 (Figure 6a and equation (1)), the coefficients of peak friction for cohesive surfaces (μ_f^p) range from 0.23 to 0.30 (Figure 6c and equation (2)). In both cases, the results suggest that the OPA fault gouges are weak compared to the Byerlee's (1978) rule.

Figure 10 shows a second comparison of peak friction values (calculated as $\mu = \frac{\tau}{\sigma_n}$), where the values of frictional strength of OPA are in concordance with other kaolinite-rich samples that have similar clay content (Behnsen & Faulkner, 2012; Bos et al., 2000; Crawford et al., 2008).

In terms of fault reactivation, unfortunately, Fang et al. (2017) performed just one test; thus, comparison is difficult. However, their results for Opalinus Clay at 3 MPa on intact material are in agreement with the trend of our results.

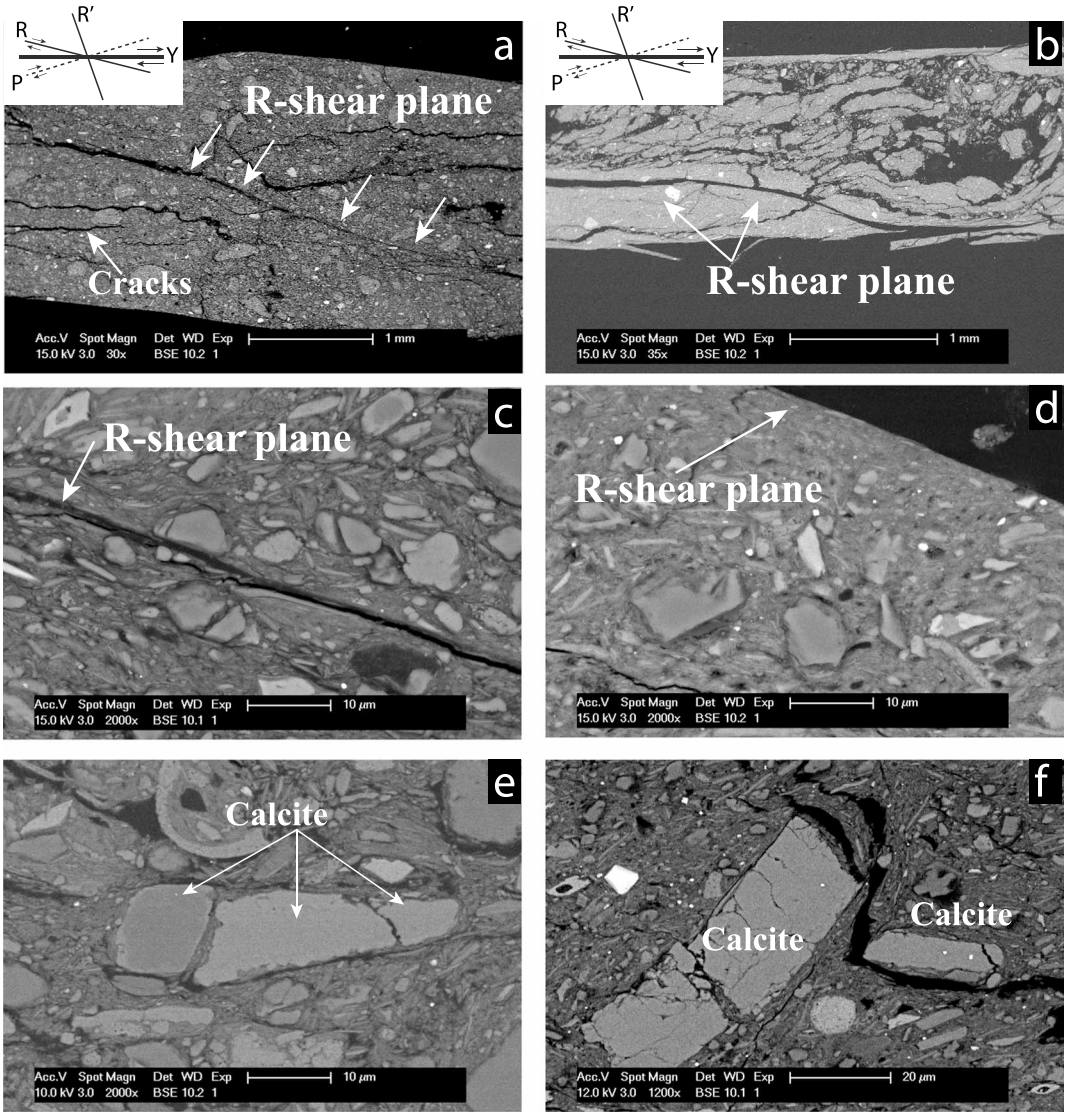

Figure 9. (a–f) BSE images of postmortem OPA samples. Shear direction is at the top of Figures 9a and 9b. The orientation of typical brittle fault zone is in included. Figures 9a, 9c, and 9e show sample sheared at 7 MPa normal stress. Figures 9b, 9d, and 9f show sample sheared at 30 MPa normal stress. R-shear plane, weak foliation, and development of cracks often aligned subparallel to the shear direction (Figure 9a). R-shear plane on sample sheared at 30 MPa (Figure 9b). Significant grain-size reduction within the entire experimental fault. Close-up of a Riedel shear plane (Figure 9c). Note the clay alignment parallel to the R-shear plane. Detailed R- shear plane on sample sheared at 30 MPa (Figure 9d). We observe a band of grain size reduction. Figures 9e and 9f show intragranular cracks in calcite minerals. The penetrative clays in the cracks suggest that microcracking occurred during deformation. Photos also show how clays flow around stiffer fragments such as calcite and quartz.

5.1.1. Variation of Friction With Normal Stress

In our experiments, we observe a reduction in peak friction (μ_{peak}), from 0.52 to 0.34, and steady state friction (μ_{ss}), from 0.37 to 0.29 with increasing normal stress from 4 to 30 MPa (Figure 6a). This similar behavior has already been observed in direct shear tests on other types of clay-rich samples, such as Ca-smectite and illite/smectite gouges (Ikari et al., 2007; Saffer et al., 2001; Saffer & Marone, 2003). In the same configuration, Numelin et al. (2007) reported a decrease of ~50% of the peak friction coefficient from normal stress of 5 MPa to 100 MPa in samples containing >50% clay content (smectite/illite −32%, muscovite −25%). Similarly, Behnsen and Faulkner (2012) reported saw-cut tests where peak friction coefficients decrease with increasing normal stress for several phyllosilicates gouges. Among them, kaolinite-rich gouges experienced a reduction of peak friction from 0.35 to 0.25 when sheared at 5 and 50 MPa normal stresses, respectively (Figure 10).

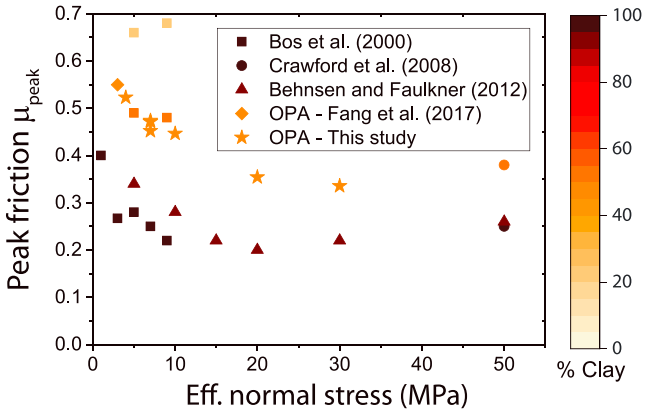

Figure 10. Comparison of the peak coefficient of friction as a function of effective normal stress for different kaolinite-rich clay gouges.

Different processes have been evoked to explain the decrease of friction with increasing normal stress. For instance, Saffer and Marone (2003) argued the possibility of water flowing into pore spaces resulting in undetected high pore pressures during the experiment. A second hypothesis presented by the same authors referred to a progressive increase of contact area between grains with increasing normal stress until a constant value of contact area at higher stress (>40 MPa). Behnsen and Faulkner (2012) argued consolidation and squeezing of water, promoting mineral to mineral contact due to a reduction in pore space. In addition, the same authors discussed about the role of gouge "cohesion" as a speculative explanation for an overestimation of friction at low normal stress ($\sigma_n < 20$ MPa).

We have tested the cohesion hypothesis, so we calculated both the friction coefficient (μ) and the friction coefficient for cohesive surface μ_f (Figure 6c and equation (2)). The steady state coefficients of friction μ_f^{ss} do not vary with normal stress confirming that gouge cohesion produce an apparent increase in friction at low normal stress (Figure 6c). However, the coefficients of friction at peak strength μ_f^p depend on normal stress (Figure 6c). Therefore, gouge cohesion can only partially explain the decrease of the (Amonton's) friction coefficient with increasing normal stress (Figure 6a).

Based on our results, we suggest that this dependency is the result of (1) the different initial porosities and (2) the amount of consolidation experienced during shearing (Figure 8a). Before shearing, saturated samples compacted at high normal stress (20 and 30 MPa) have lower porosity (low water content) compared with samples compacted at lower normal stresses (4 and 7 MPa). Indeed, before shearing, samples had different initial thickness because of compaction at various normal stresses: ~2.7 mm on average for samples sheared at 4 and 7 MPa and ~2.25 mm on average for samples sheared at >10 MPa. Accordingly, initial porosities for samples sheared at 4 and 7 MPa was of about ~27, while ~22% for samples sheared at 10, 20, and 30 MPa. Our values are in agreement with oedometric tests of powdered Opalinus Clay (Favero et al., 2016). Moreover, Figure 4 shows different slopes during the quasi-linear loading of the samples, posing a correlation between stiffer samples, i.e., steeper slopes, and low porosity samples (Figure 8c).

High porosity samples (4 and 7 MPa) are less dense and grains more spaced and will therefore deform to large strains without pervasive fracturing as shown in the microstructures (Figure 9a). Thus, grains will tend to easily slide over each other and rotate (Figure 9c). Moreover, limited grain size reduction will take place as observed in our microstructures. On the other hand, low porosity samples (>10 MPa) might have a smaller pore structure and the sample will have to dilate or grains will have to crack in order for movement to occur (Figure 9f). Thus, pervasive cataclasis will take place, including grain size reduction, microcracking, a higher number, and more well-developed Riedel planes as observed in sample sheared at 30 MPa normal stress (Figure 9b).

These observations are also compatible with the slip weakening (Figure 4) found immediately after peak shear strength (τ_{peak}) at low normal stress (4 and 7 MPa). Indeed, this decrease is about 36% for samples sheared at 4 and 7 MPa and ~13% for samples sheared at 20 and 30 MPa. The latter confirms a significant slip weakening effect, resulting in a strong to moderate strength drop over millimeter-scale slip distances.

Finally, based on microstructures and mechanical data, we suggest a transition in the relative importance of the shear deformation mechanisms operating over the whole range of normal stress. The transition occurs at normal stresses higher than 10 MPa (Figure 6) as a result of a change in mechanical behavior from deformation, mainly accommodated by frictional sliding (grain sliding, rotation, and translation of minerals) and minor fracturing within the clay matrix (at low normal stress <10 MPa), to a combination of frictional sliding and strong fracturing (at high normal stress >10 MPa).

5.1.2. Influence of Water on Frictional Strength

The peak friction coefficient for dry OPA is 0.57, while for the wet samples sheared at the same normal stress (7 MPa), it is about 0.47. Similarly, previous experiments comparing dry versus saturated friction show higher friction values for dry samples than for saturated samples (Behnsen & Faulkner, 2012; Crawford et al., 2008; Moore & Lockner, 2004). Because of the sheet structure of clay minerals, platy phyllosilicates separated by

water layers may allow shear to be concentrated within the water layers, which results in a substantial decrease of friction coefficient (Moore & Lockner, 2004). Thus, friction might increase with the total loss of water between mineral surfaces, and the upper limit of frictional strength of phyllosilicate gouges would be the strength of each mineral under dry conditions (Behnsen & Faulkner, 2012). The tendency to adsorb water has been attributed to (1) surface charge, i.e., hydrophilic versus hydrophobic surfaces; (2) the chemistry and pH of the water; and (3) pressure-temperature conditions (Morrow et al., 2000).

We have performed dry and wet experiments at 7 MPa of normal stress at the same pressure and temperature conditions. We have used water at chemical equilibrium to minimize the effects of water chemistry changes due to buffering from interaction with the simulated gouge. Therefore, we suggest that the reduction of frictional strength can only be explained by the different surface charge capacities of the clays minerals of OPA (kaolinite, chlorite, mica, and illite/smectite). A detailed analysis of the contribution of each clay is out of the scope of this paper.

5.2. Fault Stability

The frictional rate parameter ($a - b$) of OPA that ranges between 0.0012 to 0.0072 shows similar values when compared to other types of rocks with >40 wt % clays (Ikari, Saffer, & Marone, 2009; Kohli & Zoback, 2013; Numelin et al., 2007; Tembe et al., 2010). At 25 MPa normal stress, experiments on natural samples containing kaolinite (25% chlorite + kaolinite), taken from the Northeast Boundary Fault (San Andres Fault), have shown a velocity strengthening regime with values of ($a - b$) of about 0.004–0.0055 (Carpenter et al., 2015). Similarly, the friction parameter ($a - b$) of OPA indicates same velocity strengthening regime but with slightly lower values ranging from 0012 to 0.0041 at both 20 and 30 MPa.

The friction parameters ($a - b$) decrease as normal stress increases (Figure 7a). In particular, in our experiments, ($a - b$) decreases with increasing normal stress as result of the increase in the friction rate parameter b and constant values of friction parameter a (Figure 7b). On saturated samples, no transition from velocity strengthening to velocity weakening is observed as well as no clear dependency on sliding velocity.

The direct effect a is interpreted as the effect of loading rate on asperity strength with relatively constant contact area (Paterson & Wong, 2005). Despite difficulties to account for a physical interpretation of this value, dilation has been found to have a partial correlation to the magnitude of the parameter a (Scholz, 2002). In our experiments, the friction parameter a is constant with respect to normal stress (Figure 7b), and we do not observe an apparent dependency on the sliding velocities. Thus, we do not observe any apparent correlation between dilation and a.

The evolution of the parameter b can be interpreted as the changes in asperities contact sizes due to the changes in strength during the lifetime of an asperity i.e., a decrease in contact area upon a change (increase) in sliding velocity (Niemeijer et al., 2010; Paterson & Wong, 2005; Scholz, 2002). The critical slip distance D_c is the slip required to replace an entire population of asperity contacts; thus, the memory of prior state is removed (Paterson & Wong, 2005).

At the same normal stress, we do not observe an explicit dependency of parameter b with increasing up-step sliding velocities (Figure 7b), suggesting that contact area does not strongly change after variations in a velocity step. On the other hand, the increase of b values with normal stress (<10 MPa) might be explained by the lower porosities and the lower state of localization in samples sheared at 4 and 7 MPa, as indicated by the values initial porosity (Figure 8a) and the microstructures of those samples (Figure 9). At normal stress higher than 10 MPa, b values are relatively constant (0.002–0.004) and do not change with increasing normal stress. This behavior is in agreement with the evolution of critical slip distance D_c (Figure 7c).

5.3. Fault Healing

Frictional healing is a time- and slip-dependent mechanism related to fault strengthening between interseismic periods. Frictional healing depends on the mechanical and physicochemical processes at asperity contacts based on factors such as temperature, pressure, porosity, grain size distribution, and shape (Marone, 1998; Niemeijer et al., 2008; Renard et al., 2012; Yasuhara et al., 2005). Under quasi-stationary contact, the static coefficient of friction increases with time, and this time-dependent strengthening or aging effect is characterized by the healing rate β (equation (6)) (Paterson & Wong, 2005).

Among fault rocks, phyllosilicates are characterized by their small healing values ($\Delta\mu$) and healing rates (β) (Bos et al., 2000; Carpenter et al., 2016; Haines et al., 2014) when compared to other granular materials such as quartz or calcite-rich rocks.

During our slide-hold-slide tests, we calculated values of healing ($\Delta\mu$) very close to zero (Figure 7d), i.e., a negligible restrengthening after quasi-stationary contact (i.e., hold period) and small healing rates (β). This lack fault restrengthening has, indeed, important implications to the slip behavior of this fault. As the fault will not be able to regain its strength (or part of it) during the interseismic periods, the fault will not slide seismically, therefore resulting in long-term stable fault creeping. Our results are in concordance with the idea that clay minerals may act as inhibitors to contact strengthening (Bos & Spiers, 2000; Niemeijer & Spiers, 2006) and with previous work reported on clay-rich gouges (Carpenter et al., 2011; Chen et al., 2015; Tesei et al., 2012).

When samples were sheared at $\sigma_n > 10$ MPa, frictional healing values remained constantly positive (Figure 7d) and are linearly proportional to the logarithm of time. However, samples sheared at 4 and 7 MPa normal stress reveal a "parabolic" frictional healing transition, from negative ($\Delta\mu^-$) to positive ($\Delta\mu^+$) healing values.

To better constrain our results, we have performed an additional experiment to explore the role of water in healing properties of Opalinus Clay gouge. We have carried out an additional test at 7 MPa normal stress, following the same experimental procedure described before, but under controlled dry conditions (5% RH). Contrary to wet samples, dry OPA shows only a positive frictional healing rate ($\beta_{dry} \approx 0.0006$), revealing the importance of water on the healing behavior of OPA.

We propose a mechanism where water-filling pores may experience local overpressure because of compaction of the gouges when sliding resumes after the short hold times (<300 s). Because there is no time for water diffusion to occur, probably helped by some low permeability of the material, undrained reshearing will raise up pore pressure decreasing effective normal stress resulting in null or negative frictional healing.

For longer holding times (>300 s), water may be expelled, thus preventing the attainment of fluid overpressure and leading to restrengthening (positive healing rates) as we observe. Because initial sample compaction is lower at low rather than at high normal stress (see Figure 8a), the expulsion of water might be stronger just in samples sheared at 4 and 7 MPa normal stress, as they are more likely to further compact during shearing.

Based on a simple form, we estimate the time constant (Wang, 2000) for water diffusion $t_d \approx \frac{L^2}{4c}$, where c $\left(\frac{mm^2}{s}\right)$ is the hydraulic diffusivity and L is the maximum path length (mm). We deduced values of powdered Opalinus Clay, i.e., crushed and then molded, for the hydraulic diffusivity at different normal stress (Favero et al., 2016). We calculated t_d using $L = 25$ mm, the maximum path length of diffusion (half length of the samples). Values of hydraulic diffusivity decreased from 0.23 to 0.12 mm^2/s as long normal stresses increased. Then, we found $t_d \approx 700$ s for samples sheared at 4 and 7 MPa normal stress (Figure 8b). The previous analysis is consistent with the hold times $t_h^* = 300$ s presented in the results section. Since we used the maximum length of the fluid path, these values correspond to maximum diffusion times during hold times. Considering the uncertainty in both diffusion coefficient and the actual diffusion path length, this calculation suggests that water diffusion promoting frictional strengthening is keen to play a role in the observed healing behavior.

However, if local overpressures played a role upon reshearing during slide hold slide tests, it will also affect the results of the velocity steps. In particular, it will affect the results during sliding at faster up-step velocities (>30 μm/s) when pore water has absolutely no time to diffuse ($t \approx 2$ s for up-step velocity of 300 μm/s). However, we have not observed any correlation of the friction parameter ($a - b$) with respect to up-step velocity (Figure 7a), suggesting that local fluid overpressure is not a very active process during velocity steps and maybe it is not the only one acting during the frictional healing of OPA.

A second hypothesis we suggest is a competition between two mechanisms: consolidation and the creation of local swelling pressures. The global trend of porosity ($\varnothing_t$) indicates that samples compacted on shearing (Figure 8a) during our experiments. In particular, during slide-hold-slide tests, samples experienced compaction on shearing and null dilation during hold times (Figure 8c). However, when we removed the linear trend from the total porosity calculations, we do observe a small influence of dilation. Despite dilation is minimum in our tests, it appears more marked in samples sheared at 4 and 7 MPa than in samples sheared at 10, 20, and 30 MPa. Indeed, the higher rate of porosity ($\varnothing_c$) changes of sample sheared at low normal stress is in concordance with this observation (Figure 8c).

Following our argument, we assumed that the dilation experienced by our samples may correspond to local swelling pressures of some clay minerals that operate at different rates with respect to normal stress. Because swelling pressures of OPA are up to ~6 MPa (Zhang, Wieczorek, et al., 2010), its effect will be more significant for samples sheared at low normal stress, (4,7 MPa) than at high normal stress (10, 20, and 30 MPa). Thus, at low normal stress, a strong competition between shear consolidation and swelling pressures takes place, but swelling pressures play a more important role, being responsible for the reduction in frictional strength i.e., negative healing values, observed in our samples. For hold times >300 s, consolidation (as observed in the total porosity $\varnothing_t$) leads to densification of the samples, requiring dilation upon reshearing promoting the restrengthening of the samples. For samples sheared at high normal stress, dilation is null, so if swelling pressures operate, their effect is negligible.

A third hypothesis we propose is that water has a mechanical lubricating effect preventing the restrengthening of OPA (Behnsen & Faulkner, 2012; Moore & Lockner, 2004; Morrow et al., 2000; Renard et al., 2012). In the saturated gouges, water forms a thin film in proportion to the surface energy properties of the clays (Moore & Lockner, 2004), but also, as a function of contact normal stress, salinity, and temperature (Renard & Ortoleva, 1997). Indeed, the water film thickness at grain to grain contacts decreases with increasing normal load (Renard & Ortoleva, 1997), supporting the observations in our tests that the healing behavior is also function of normal stress. The latter is also consistent with the fact that samples sheared at low normal stress have a higher porosity than samples sheared at 10, 20, and 30 MPa. As in the second hypothesis, for hold times >300 s, the increase of packing density controls the restrengthening of the samples.

Although these weakening mechanisms are a reasonable explanation for the healing behavior experienced by our samples, other mechanisms affecting friction are also possible. Some of them could be the relative electrochemical effect of the other clays (smectite, chlorite, and illite) presented in OPA (Behnsen & Faulkner, 2012; Morrow et al., 2000), disjoining pressures (Gonçalvès et al., 2010), saturation of contact area (Ikari et al., 2009), pressure solution (Yasuhara et al., 2005; Zhang, Spiers, et al., 2010), thermal expansion by local temperature increase (even though room temperature was constant), a combination of two or more of the previous mechanism, etc.; the future, dedicated experiments to understand this negative healing behavior will be performed by varying the viscosity and the chemistry of the fluid.

5.4. Implications for Nuclear Waste Storage

Our experiments on fault gouge derived from the Opalinus Clay formation have documented a very low frictional strength at different normal stress (4–30 MPa). As normal stress increased, the associated mechanical deformation mechanism evolves from deformation mainly accommodated by frictional sliding and minor (at low normal stress <10 MPa) to major and pervasive fracturing (at high normal stress >10 MPa).

A key observation of this study is that upon fault reactivation, the velocity strengthening behavior observed at different normal stress suggests stable sliding as the most likely fault slip-behavior. In addition, our results indicate that the healing behavior of the fault is dominated by a lack of restrengthening during interseismic periods. Therefore, we propose that if a fault system within the Opalinus Clay formation reactivates (at the hypothetic boundary conditions for a nuclear waste repository: conditions imposed during experiments, i.e., crustal depth of 150–1,000 m and no fluid pressure), it will reactivate within the aseismic regime and earthquakes might be difficult to nucleate. Moreover, the absence of long-term interseismic healing will prevent the fault from re-gaining fault strength, resulting in stable fault creeping.

Even though our previous results suggest aseismic creep, departures from this behavior can be induced by (1) the attainment of fluid overpressure that can change the frictional rheology of the fault (Scuderi & Collettini, 2016), (2) coseismic slip if a dynamic rupture from a large earthquake propagates onto saturated clay-rich faults (Bullock et al., 2015; Faulkner et al., 2011), and (3) an abrupt perturbation of the surrounding stress field caused by natural or anthropogenic operations (Perfettini & Ampuero, 2008).

6. Conclusions

We have systematically tested the frictional behavior of water-saturated Opalinus Clay formation performing double-direct shear experiments at normal stress ranging from 4 to 30 MPa and sliding velocity between 1 and 300 μm/s. Slide-hold-slide tests (1–3,000 s) have been carried out to analyze the healing capacity of fault in OPA formation. Our results indicate the following: (1) very low peak and steady state friction; (2) moderate

slip weakening at normal stress lower than 10 MPa; (3) velocity strengthening behavior at all normal stresses, with the friction rate parameter ($a - b$) that decreases increasing normal stress; and (4) almost zero healing values at different hold periods and normal stresses

These results suggest that OPA faults are mechanically weak, and due to the low frictional healing, they remain weak in the long term. Moreover, our results suggest that faults within the Opalinus Clay formation can be easily reactivated during stress and hydro-mechanical perturbations, predominantly with aseismic creep as inferred by the velocity strengthening behavior of the fault rocks and the lack of restrengthening during inter-seismic periods.

Our results also reveal conditions for potential frictional slip instability at very shallow depths (~150 m), as the mechanical behavior of the fault system presents moderate evidence of slip weakening behavior. In the framework of deep geological disposal in clay formations, the most promising option for deep geological nuclear waste storage, our results indicate that stable slip within the fault structure is the most likely slip behavior. However, the interaction of the fault behavior with anthropogenic operations put the long-term safety into question due to reactivation during stress and hydro-mechanical perturbations.

Acknowledgments
We acknowledge the many researchers for helping us to develop this research: Christophe Nussbaum for funding through Swisstopo and Yves Guglielmi providing access to the samples, Carolina Giorgetti for helping on the data processing, Laurent Gastaldo and Benjamin Frey for sample preparation, Thierry Adatte for XRD measurements, and Piergiorgio Scarlato for allowing us to run the experiments at INGV. Jean François Molinari and Brett Carpenter are thanked for fruitful discussions. Finally, we want to thank André Niemeijer, Nicola De Paola, and an anonymous reviewer for their constructive review, which helped improved this paper. M.V. and L.F.O. thank EPFL for the financial support. The data sets analyzed during the current study are available in the EPFL-ENAC repository, [https://enacshare.epfl.ch/d4iE9VfNs63PkxnUJrF2M]. In addition, raw data can be requested to felipe.orellana@epfl.ch.

References

Behnsen, J., & Faulkner, D. R. (2012). The effect of mineralogy and effective normal stress on frictional strength of sheet silicates. *Journal of Structural Geology*, *42*, 49–61. https://doi.org/10.1016/j.jsg.2012.06.015

Bird, P. (1984). Hydration-phase diagrams and friction of montmorillonite under laboratory and geologic conditions, with implications for shale compaction, slope stability, and strength of fault gouge. *Tectonophysics*, *107*(3–4), 235–260. https://doi.org/10.1016/0040-1951(84)90253-1

Bock, H., Dehandschutter, B., Martin, C. D., Mazurek, M., De Haller, A., Skoczylas, F., & Davy, C. (2010). Seal-sealing of fractures in argillaceous formations in the context of geological disposal of radioactive waste: Review and Synthesis, Nuclear Energy Agency - Organization for Economic Co-Operation and Development.

Bos, B., Peach, C. J., & Spiers, C. J. (2000). Frictional-viscous flow of simulated fault gouge caused by the combined effects of phyllosilicates and pressure solution. *Tectonophysics*, *327*(3–4), 173–194. https://doi.org/10.1016/S0040-1951(00)00168-2

Bos, B., & Spiers, C. J. (2000). Effect of phyllosilicates on fluid-assisted healing of gouge-bearing faults. *Earth and Planetary Science Letters*, *184*(1), 199–210. https://doi.org/10.1016/S0012-821X(00)00304-6

Bossart, P., Bernier, F., Birkholzer, J., Bruggeman, C., Connolly, P., Dewonck, S., … Wieczorek, K. (2017). Mont Terri rock laboratory, 20 years of research: introduction, site characteristics and overview of experiments. *Swiss Journal of Geosciences*, *110*(1), 3–22. https://doi.org/10.1007/s00015-016-0236-1

Brantut, N., Schubnel, A., Rouzaud, J. N., Brunet, F., & Shimamoto, T. (2008). High-velocity frictional properties of a clay-bearing fault gouge and implications for earthquake mechanics. *Journal of Geophysical Research*, *113*, B10401. https://doi.org/10.1029/2007JB005551

Bullock, R. J., De Paola, N., & Holdsworth, R. E. (2015). An experimental investigation into the role of phyllosilicate content on earthquake propagation during seismic slip in carbonate faults. *Journal of Geophysical Research: Solid Earth*, *120*, 3187–3207. https://doi.org/10.1002/2015JB011914

Byerlee, J. D. (1978). Friction of rocks. *Pure and Applied Geophysics*, *116*(4–5), 615–626. https://doi.org/10.1007/BF00876528

Carpenter, B. M., Ikari, M. J., & Marone, C. (2016). Laboratory observations of time-dependent frictional strengthening and stress relaxation in natural and synthetic fault gouges. *Journal of Geophysical Research: Solid Earth*, *121*, 1183–1201. https://doi.org/10.1002/2015JB012136. Received

Carpenter, B. M., Marone, C., & Saffer, D. (2011). Weakness of the San Andreas Fault revealed by samples from the active fault zone. *Nature Geoscience*, *4*(4), 251–254. https://doi.org/10.1038/ngeo1089

Carpenter, B. M., Saffer, D., & Marone, C. (2015). Frictional properties of the active San Andreas Fault at SAFOD: Implications for fault strength and slip behavior. *Journal of Geophysical Research: Solid Earth*, *120*, 5273–5289. https://doi.org/10.1002/2015JB011963

Chen, J., Verberne, B. A., & Spiers, C. J. (2015). Effects of healing on the seismogenic potential of carbonate fault rocks: Experiments on samples from the Longmenshan Fault, Sichuan, China. *Journal of Geophysical Research: Solid Earth*, *120*, 5479–5506. https://doi.org/10.1002/2015JB012051

Collettini, C., Di Stefano, G., Carpenter, B. M., Scarlato, P., Tesei, T., Mollo, S., … Chiaraluce, L. (2014). A novel and versatile apparatus for brittle rock deformation. *International Journal of Rock Mechanics and Mining Sciences*, *66*, 114–123. https://doi.org/10.1016/j.ijrmms.2013.12.005

Crawford, B., Faulkner, D. R., & Rutter, E. H. (2008). Strength, porosity, and permeability development during hydrostatic and shear loading of synthetic quartz-clay fault gouge. *Journal of Geophysical Research*, *113*, B03207. https://doi.org/10.1029/2006JB004634

Dieterich, J. H. (1979). Modeling of rock friction: 1. Experimental results and constitutive equations. *Journal of Geophysical Research*, *84*, 2161–2168. https://doi.org/10.1007/BF00876539

Fang, Y., Elsworth, D., Wang, C., Ishibashi, T., & Fitts, J. P. (2017). Frictional stability-permeability relationships for fractures in shales. *Journal of Geophysical Research: Solid Earth*, *122*, 1760–1776. https://doi.org/10.1002/2016JB013435

Faulkner, D. R., Mitchell, T. M., Behnsen, J., Hirose, T., & Shimamoto, T. (2011). Stuck in the mud? Earthquake nucleation and propagation through accretionary forearcs. *Geophysical Research Letters*, *38*, L18303. https://doi.org/10.1029/2011GL048552

Favero, V., Ferrari, A., & Laloui, L. (2016). On the hydro-mechanical behavior of remolded and natural Opalinus Clay shale. *Engineering Geology*, *208*, 128–135. https://doi.org/10.1016/j.enggeo.2016.04.030

Gonçalvès, J., Rousseau-Gueutin, P., De Marsily, G., Cosenza, P., & Violette, S. (2010). What is the significance of pore pressure in a saturated shale layer? *Water Resources Research*, *46*, W04514. https://doi.org/10.1029/2009WR008090

Haines, S. H., Marone, C., & Saffer, D. (2014). Frictional properties of low-angle normal fault gouges and implications for low-angle normal fault slip. *Earth and Planetary Science Letters*, *408*, 57–65. https://doi.org/10.1016/j.epsl.2014.09.034

Hashash, Y. M. A., Hook, J. J., Schmidt, B., & Yao, J. I.-C. (2001). Seismic design and analysis of underground structures. *Tunnelling and underground space technology*, *16*(4), 247–293. https://doi.org/10.1016/S0886-7798(01)00051-7

Ikari, M. J., Marone, C., & Saffer, D. (2011). On the relation between fault strength and frictional stability. *Geology*, *39*(1), 83–86. https://doi.org/10.1130/G31416.1

Ikari, M. J., Saffer, D., & Marone, C. (2007). Effect of hydration state on the frictional properties of montmorillonite-based fault gouge. *Journal of Geophysical Research*, *112*, B06423. https://doi.org/10.1029/2006JB004748

Ikari, M. J., Saffer, D., & Marone, C. (2009). Frictional and hydrologic properties of clay-rich fault gouge. *Journal of Geophysical Research*, *114*, B05409. https://doi.org/10.1029/2008JB006089

Klinkenberg, M., Kaufhold, S., Dohrmann, R., & Siegesmund, S. (2009). Influence of carbonate microfabrics on the failure strength of claystones. *Engineering Geology*, *107*(1–2), 42–54. https://doi.org/10.1016/j.enggeo.2009.04.001

Kohli, A. H., & Zoback, M. D. (2013). Frictional properties of shale reservoir rocks. *Journal of Geophysical Research: Solid Earth*, *118*, 5109–5125. https://doi.org/10.1002/jgrb.50346

Kübler, B. (1987). Cristallinité de l'illite, méthodes normalisées de préparations, méthodes normalisées de mesures. *Cahiers de l'Institut de Géologie de Neuchâtel, Série ADX*, *1*, 13.

Laurich, B., Urai, J. L., Desbois, G., Vollmer, C., & Nussbaum, C. (2014). Microstructural evolution of an incipient fault zone in Opalinus Clay: Insights from an optical and electron microscopic study of ion-beam polished samples from the Main Fault in the Mt-Terri Underground Research Laboratory. *Journal of Structural Geology*, *67*(PA), 107–128. https://doi.org/10.1016/j.jsg.2014.07.014

Lockner, D. A., & Beeler, N. (2002). Rock failure and earthquakes. In W. H. K. Lee, et al. (Eds.), *International handbook of earthquake and seismology. Part A* (pp. 505–537). Amsterdam: Academic Press.

Logan, J. M., Dengo, C. A., Higgs, N. G., & Wang, Z. Z. (1992). Chapter 2 Fabrics of experimental fault zones: Their development and relationship to mechanical behavior. *International Geophysics.*, *51*(C), 33–67. https://doi.org/10.1016/S0074-6142(08)62814-4

Marone, C. (1998). Laboratory-Derived Friction Laws and Their Application To Seismic Faulting. *Annual Review of Earth and Planetary Sciences*, *26*(1), 643–696. https://doi.org/10.1146/annurev.earth.26.1.643

Moore, D. E., & Lockner, D. A. (2004). Crystallographic controls on the frictional behavior of dry and water-saturated sheet structure minerals. *Journal of Geophysical Research*, *109*, B03401. https://doi.org/10.1029/2003JB002582

Morrow, C., Moore, D. E., & Lockner, D. A. (2000). The effect of mineral bond strength and adsorbed water on fault gouge frictional strength. *Geophysical Research Letters*, *27*, 815–818. https://doi.org/10.1029/1999GL008401

Niemeijer, A. R., & Collettini, C. (2013). Frictional properties of a low-angle normal fault under in situ conditions: Thermally-activated velocity weakening. *Pure and Applied Geophysics*, *171*(10), 2641–2664. https://doi.org/10.1007/s00024-013-0759-6

Niemeijer, A. R., Marone, C., & Elsworth, D. (2008). Healing of simulated fault gouges aided by pressure solution: Results from rock analogue experiments. *Journal of Geophysical Research*, *113*, B04204. https://doi.org/10.1029/2007JB005376

Niemeijer, A. R., Marone, C., & Elsworth, D. (2010). Frictional strength and strain weakening in simulated fault gouge: Competition between geometrical weakening and chemical strengthening. *Journal of Geophysical Research*, *115*, B10207. https://doi.org/10.1029/2009JB000838

Niemeijer, A. R., & Spiers, C. J. (2006). Velocity dependence of strength and healing behavior in simulated phyllosilicate-bearing fault gouge. *Tectonophysics*, *427*(1–4), 231–253. https://doi.org/10.1016/j.tecto.2006.03.048

Numelin, T., Marone, C., & Kirby, E. (2007). Frictional properties of natural fault gouge from a low-angle normal fault, Panamint Valley, California. *Tectonics*, *26*, TC2004. https://doi.org/10.1029/2005TC001916

Nussbaum, C., Bossart, P., Amann, F., & Aubourg, C. (2011). Analysis of tectonic structures and excavation induced fractures in the Opalinus Clay, Mont Terri underground rock laboratory (Switzerland). *Swiss Journal of Geosciences*, *104*(2), 187–210. https://doi.org/10.1007/s00015-011-0070-4

Passchier, C. W., & Trouw, R. R. A. J. (2005). Microtectonics.

Paterson, M. S., & Wong, T. F. (2005). *Experimental rock deformation—The brittle field* (2nd ed.). Berlin: Springer-Verlag.

Perfettini, H., & Ampuero, J. P. (2008). Dynamics of a velocity strengthening fault region: Implications for slow earthquakes and postseismic slip. *Journal of Geophysical Research*, *113*, B09411. https://doi.org/10.1029/2007JB005398

Popp, T., Salzer, K., & Minkley, W. (2008). Influence of bedding planes to EDZ-evolution and the coupled HM properties of Opalinus Clay. *Physics and Chemistry of the Earth*, *33*(SUPPL. 1), 374–387. https://doi.org/10.1016/j.pce.2008.10.018

Rabinowicz, E. (1951). The nature of the static and kinetic coefficients of friction. *Journal of Applied Physics*, *22*(11), 1373–1379. https://doi.org/10.1063/1.1699869

Reinen, L. A., & Weeks, J. D. (1993). Determination of rock friction constitutive parameters using an iterative least squares inversion method. *Journal of Geophysical Research*, *98*, 15,937–15,950. https://doi.org/10.1029/93JB00780

Renard, F., Beauprêtre, S., Voisin, C., Zigone, D., Candela, T., Dysthe, D. K., & Gratier, J. P. (2012). Strength evolution of a reactive frictional interface is controlled by the dynamics of contacts and chemical effects. *Earth and Planetary Science Letters*, *341–344*, 20–34. https://doi.org/10.1016/j.epsl.2012.04.048

Renard, F., & Ortoleva, P. (1997). Water films at grain-grain contacts: Debye-Hückel, osmotic model of stress, salinity, and mineralogy dependence. *Geochimica et Cosmochimica Acta*, *61*(10), 1963–1970. https://doi.org/10.1016/S0016-7037(97)00036-7

Ruina, A. (1983). Slip instability and state variable friction laws. *Journal of Geophysical Research*, *88*, 10359. https://doi.org/10.1029/JB088iB12p10359

Saffer, D., Frye, K. M., Marone, C., & Mair, K. (2001). Laboratory results indicating complex and potentially unstable frictional behavior of smectite clay. *Geophysical Research Letters*, *28*, 2297–2300. https://doi.org/10.1029/2001GL012869

Saffer, D., Lockner, D. A., & McKiernan, A. (2012). Effects of smectite to illite transformation on the frictional strength and sliding stability of intact marine mudstones. *Geophysical Research Letters*, *39*, L11304. https://doi.org/10.1029/2012GL051761

Saffer, D., & Marone, C. (2003). Comparison of smectite- and illite-rich gouge frictional properties: Application to the updip limit of the seismogenic zone along subduction megathrusts. *Earth and Planetary Science Letters*, *215*(1–2), 219–235. https://doi.org/10.1016/S0012-821X(03)00424-2

Samuelson, J., Elsworth, D., & Marone, C. (2009). Shear-induced dilatancy of fluid-saturated faults: Experiment and theory. *Journal of Geophysical Research*, *114*, B12404. https://doi.org/10.1029/2008JB006273

Scholz, C. H. (1998). Earthquakes and friction laws. *Nature*, *391*(6662), 37–42. https://doi.org/10.1038/34097

Scholz, C. H. (2002). *The mechanics of earthquakes and faulting* (2nd ed.). Cambridge University Press.

Scuderi, M. M., & Collettini, C. (2016). The role of fluid pressure in induced vs. triggered seismicity: Insights from rock deformation experiments on carbonates. *Scientific Reports*, *6*(1), 24852. https://doi.org/10.1038/srep24852

Shimamoto, T., & Logan, J. M. (1981). Effects of simulated clay gouges on the sliding behavior of Tennessee sandstone. *Tectonophysics*, *75*(3–4), 243–255. https://doi.org/10.1016/0040-1951(81)90276-6

Smith, S. A. F., & Faulkner, D. R. (2010). Laboratory measurements of the frictional properties of the Zuccale low-angle normal fault, Elba Island, Italy. *Journal of Geophysical Research*, *115*, B02407. https://doi.org/10.1029/2008JB006274

Tembe, S., Lockner, D. A., & Wong, T. F. (2010). Effect of clay content and mineralogy on frictional sliding behavior of simulated gouges: Binary and ternary mixtures of quartz, illite, and montmorillonite. *Journal of Geophysical Research*, *115*, B03416. https://doi.org/10.1029/2009JB006383

Tesei, T., Collettini, C., Barchi, M. R., Carpenter, B. M., & Di Stefano, G. (2014). Heterogeneous strength and fault zone complexity of carbonate-bearing thrusts with possible implications for seismicity. *Earth and Planetary Science Letters*, *408*, 307–318. https://doi.org/10.1016/j.epsl.2014.10.021

Tesei, T., Collettini, C., Carpenter, B. M., Viti, C., & Marone, C. (2012). Frictional strength and healing behavior of phyllosilicate-rich faults. *Journal of Geophysical Research*, *117*, B09402. https://doi.org/10.1029/2012JB009204

Tsang, C. F., Barnichon, J. D., Birkholzer, J., Li, X. L., Liu, H. H., & Sillen, X. (2012). Coupled thermo-hydro-mechanical processes in the near field of a high-level radioactive waste repository in clay formations. *International Journal of Rock Mechanics and Mining Sciences*, *49*, 31–44. https://doi.org/10.1016/j.ijrmms.2011.09.015

Tsutsumi, A., Fabbri, O., Karpoff, A. M., Ujiie, K., & Tsujimoto, A. (2011). Friction velocity dependence of clay-rich fault material along a megasplay fault in the Nankai subduction zone at intermediate to high velocities. *Geophysical Research Letters*, *38*, L19301. https://doi.org/10.1029/2011GL049314

Wang, H. F. (2000). *Theory of linear poroelasticity with applications to geomechanics and hydrogeology*. Princeton, NJ: Princeton University Press.

Wang, W. L., Wang, T. T., Su, J. J., Lin, C. H., Seng, C. R., & Huang, T. H. (2001). Assessment of damage in mountain tunnels due to the Taiwan Chi-Chi Earthquake. *Tunn. Undergr. Sp. Technol.*, *16*(3), 133–150. https://doi.org/10.1016/S0886-7798(01)00047-5

Yasuhara, H., Marone, C., & Elsworth, D. (2005). Fault zone restrengthening and frictional healing: The role of pressure solution. *Journal of Geophysical Research*, *110*, B06310. https://doi.org/10.1029/2004JB003327

Zhang, C. L., Wieczorek, K., & Xie, M. L. (2010). Swelling experiments on mudstones. *Journal of Rock Mechanics and Geotechnical Engineering*, *2*(1), 44–51. https://doi.org/10.3724/SP.J.1235.2010.00044

Zhang, X., Spiers, C. J., & Peach, C. J. (2010). Compaction creep of wet granular calcite by pressure solution at 28°C to 150°C. *Journal of Geophysical Research*, *115*, B09217. https://doi.org/10.1029/2008JB005853